ARTICLE

Received 00th January 20xx,
Accepted 00th January 20xx

DOI: 10.1039/x0xx00000x

Atomically Dispersed Co^{2+} in a Redox-Active COF for Electrochemical CO_2 Reduction to Ethanol: Unravelling Mechanistic Insight through Operando Studies

Ashish Singh,[#a] Soumitra Barman,[#a] Faruk Ahamed Rahimi,[a] Anupam Dey,[a] Rohan Jena [a],Ravi Kumar,[b] Nijita Mathew,[a] Dibyendu Bhattacharyya,[b] Tapas Kumar Maji[a]*

Designing cheap, stable, and efficient electrocatalysts for selective CO_2 reduction to ethanol is a green and sustainable approach for converting greenhouse gas into value-added products. In this context, developing single-atom-based electrocatalysts (SAEs) could be advantageous because of maximum atom utilization. Here, we report the design and synthesis of a donor-acceptor-based redox-active covalent organic framework (COF), TAPA-OPE, obtained by condensation between tri-amino-triphenyl amine (TAPA) and Oligo-(p-phenyleneethynylenes) (OPE) based dialdehyde. Owing to the presence of suitable metal chelating sites, TAPA-OPE was utilized for covalent grafting of atomic Co^{2+} (Co-TAPA-OPE), which has been confirmed by EXAFS, HAADF-STEM, and XPS studies. The Co-TAPA-OPE acts as a stable SAE for selective reduction of the CO_2 to ethanol at -0.67 V vs. RHE. Faradaic efficiency (FE) for the ethanol formation is calculated to be 66.8%. The *in-situ* XAS study discloses that single Co-site transiently changes its oxidation state and coordination environment during electrocatalytic reduction process. Further, *in-situ* FTIR study is performed to track the intermediates during the CO_2 reduction reaction (CO_2RR), which eventually assists in elucidating the plausible reaction mechanism through Density Functional Theory (DFT).

Introduction

Increasing global CO_2 release based on the large-scale combustion of fossil fuels has led to an alarming threat to the environment and sustainable growth of the world's economy.[1, 2] Therefore, comprehending sustainable technologies for capture and conversion of CO_2 to renewable fuels and feedstocks has attracted considerable attention, aiming to mitigate the rising CO_2 concentration in the atmosphere.[3-9] The electrochemical CO_2 reduction to various products encompassing C_1 (carbon monoxide, formic acid, methane), C_2 (ethylene, ethanol) or C_3 products (propanol) by exploiting renewable electricity leads to the accumulation of intermittent electricity as the reduced product.[10, 11] However, among various possible products in electrochemical CO_2 reduction reaction (CO_2RR), C_2 products are highly sought-after due to their high commercialization value.[12] Particularly, ethanol carries a positive energy balance and is one of the largest volume organic products formed in the course of CO_2RR and, therefore, ubiquitously being utilized as a liquid fuel or fuel additive, thus, noted to be a highly demanding product during the CO_2RR.[13, 14] However, the biggest bottleneck in realizing efficient electrochemical conversion of CO_2 to ethanol lies in the formation of the C-C bond, which involves numerous intermediates and the transfer of multiple electrons and protons.[15] In this regard, designing and developing an electrocatalyst for selective reduction of CO_2 to ethanol under ambient conditions is highly desirable due to not only being biofuel as well as a green solvent but also serving for storage and distribution of carbon-based fuels and renewable feedstocks in the chemical sector. Various electrocatalysts based on transition metals (mainly Cu, Co, and Ni), metal-nitrogen-carbon (M-N-C)-type materials such as cobalt-phthalocyanine, porphyrins, Cu-Ag alloys, and Mn(II)/Ru(II) polypyridyl complexes have been examined for CO_2RR to ethanol.[16-28] However, poor catalytic performance and selectivity, high overpotential, operational costs, and durability are the major concerns that need to be addressed.[29]

Recently, covalent organic frameworks (COFs), a novel class of crystalline porous organic materials, have attracted significant attention owing to synthetic tunability, excellent stability, robustness, and permanent porosity. COFs have been employed for gas storage, separation, sensing, photocatalysis, and biomedical applications.[30-32] Further, designing and developing redox-active COFs have gained recent attention due to the possibility of electrocatalytic and energy storage applications.[33] Electroactive COFs prepared by assimilating

[a] *Molecular Materials Laboratory, Chemistry and Physics of Materials Unit, School of Advanced Materials (SAMat), Jawaharlal Nehru Centre for Advanced Scientific Research Bangalore-560064, India.*
E-mail: tmaji@jncasr.ac.in
[b] *Atomic and Molecular Physics Division, Bhabha Atomic Research Centre, Mumbai 400085, India; Homi Bhabha National Institute, Training School Complex, Anushaktinagar, Mumbai 400094, India*
Electronic Supplementary Information (ESI) available:
** Dedicated to Prof. C. N. R. Rao on the occasion of his 90th Birthday.*

redox-active organic struts are still at a primitive stage and limited to investigation of the rudimentary electrochemical processes. Furthermore, judiciously chosen organic building blocks bearing metal chelating ability in the COFs can provide a platform to anchor atomically dispersed electroactive metal ions via post-synthetic modification. Owing to the high surface area and microporosity of the resulting hybrid COFs, substrate diffusion towards the catalytic site would be accelerated and, thus, likely to exhibit significantly enhanced electrocatalytic performances towards CO_2RR.[34, 35] Recently, the fabrication of atomically dispersed metal-based electrocatalysts has gained widespread attention as they offer maximum atom utilization efficiency and display impressive heterogeneous catalytic activity with unique redox properties.[28, 36-38] However, challenges associated with stabilization as well as poor loading ability of atomically dispersed metal ions are foremost concerns that are overshadowing their applications in the realm of single atom electrocatalysts (SAEs).[39] Therefore, the complexation of electroactive 3d metal ions like Co^{2+}, Ni^{2+}, Fe^{2+}, and Cu^{2+} in the COF materials would be a novel approach and pave the way to realize COF-based single atom-driven electrocatalytic CO_2 reduction to ethanol which is yet to be documented.

Herein, we report the synthesis and characterization of a new redox-active COF (TAPA-OPE) by integrating Tris-(4-aminophenyl) amine (TAPA) and substituted Oligo-(p-phenyleneethynylenes) (OPE) based dialdehyde via Schiff base condensation (Fig. 1a, S1-S2, and Scheme S1-S2). The manifestation of metal-chelating sites was exploited for the coordinative grafting of Co^{2+} in TAPA-OPE COF to prepare Co-TAPA-OPE, with a Co loading of ~2.8 wt%. Atomic dispersion and coordination environment of Co^{2+} in the COF was confirmed by microscopic (HAADF-STEM) and spectroscopic analysis (EXAFS and XPS), respectively. The Co-TAPA-OPE shows electrocatalytic activity for CO_2RR to ethanol with a maximum Faradaic efficiency of ~ 66.8% at the potential of −0.67 V vs. RHE. Utilizing *in-situ* X-ray absorption spectroscopy (XAS), we found that under the elctrochemical conditions Co centre in Co-TAPA-OPE COF undergoes reversible structural change of Co-Complex and oxidation state change of the Co-centre which catalyses the CO_2 reduction. The analysis revealed that the Co was transiently reduced from +2 to +2-δ ($0<\delta<1$) during the catalytic reaction. Additionally, the *in-situ* FTIR experiment was performed to monitor a real time reaction progress of the CO_2RR to ethanol which indicated the formation CHO* species, a key intermediate for C_2 product formation. Further, a plausible mechanism of CO_2RR has been formulated by the Density Functional Theory (DFT) in line with the experimental results.

Results and discussion

Structural characterization of the newly synthesized TAPA-OPE COF was performed by powder X-ray diffraction (PXRD) analysis and various other spectroscopic and microscopic techniques. The PXRD pattern of the TAPA-OPE showed the crystalline nature of the material (Fig. 1b-c). The Pawley refinements of PXRD patterns of the TAPA-OPE were carried out for full profile fitting in Materials Studio 20 based on both staggered (AB) (triclinic with P1 space group) and eclipsed (AA) (trigonal with $P\bar{3}$ space group) model (Fig. 1b &S3-S4). The non-planar geometry around the central nitrogen of the TAPA unit was taken into consideration while optimizing the structure. It was observed that the staggered model was found in better agreement with the experimentally observed pattern (weighted-profile R factor R_{wp} = 3.73% and unweighted-profile R factor R_p = 2.83%) as compared to the eclipsed model (R_{wp} = 4.09% and R_p = 3.14%).[40] The long alkyl side-chain at the OPE-5 unit, as well as the non-planar geometry of TAPA is likely to be accountable for the AB stacking in TAPA-OPE COF.[41] Pawley refinement of the staggered model yielded unit cell parameters of a = 55.837 Å, b = 55.826 Å, c = 9.348 Å and α = 90.185°, β = 90.048°, γ = 119.661°. TAPA-OPE COF exhibited diffraction peaks at 2θ = 3.15, 4.21, 5.76, 6.41, 7.22, 8.51, 10.81, 12.50 and 14.52° (Fig. 1c), corresponding to the (110), (200), (210), (300), (220), (410), (121), (321) and (341) facets, respectively. It should be noted that the interlayer distance could not be fixed from the experimental PXRD data due to the broad peak in the range of 2θ = 17-25°, likely to be due to the non-planarity brought in the system (TAPA-OPE) by the TAPA unit and alkyl chain of the OPE unit. Moreover, it was set to be 4.65 Å by force-field-based calculations.

Further, FTIR spectra of TAPA-OPE showed a peak at 1618 cm^{-1}, which is a characteristic peak for the imine bond (-C=N-), indicating the Schiff base condensation reaction for polymer formation (Fig. S5).[42] A distinguished peak for alkyne bond (-C≡C-) appeared at 2205 cm^{-1}, ensuring the presence of OPE-5 unit in the polymer. Solid-state ^{13}C NMR revealed peaks between 14-69 ppm for TAPA-OPE that can be attributed to the alkyl/alkoxy carbon chain substitution of the OPE-5 unit (Fig. 1e).[42] Further, peaks at 84 and 92 ppm were attributed to the alkyne bond (-C≡C-) of the OPE-5 unit. Peaks between 115-146 ppm were attributed to the aromatic rings of TAPA and OPE-5 units. Notably, a characteristic peak for imine carbon (-C=N-) appeared at 154 ppm, confirming the TAPA-OPE was formed by the Schiff base condensation.[42] Thermogravimetric analysis (TGA) showed stability of the TAPA-OPE up to 345 °C (Fig. S6). TAPA-OPE was activated at 150 °C for 24 h prior to the N_2 adsorption study at 77K. The activated COF showed type-I sorption profile, indicating the microporous nature of the polymer (Fig. 1d).[43] The BET surface area was found to be 391 m^2/g, and the pore size centered at 1.39 nm as calculated by the nonlocal density functional theory (NL-DFT) method (Fig. S7). Morphology of the TAPA-OPE was investigated by Field Emission Scanning Electron Microscopy (FESEM) and Transmission Electron Microscopy (TEM). FESEM images showed irregular elongated sheet like morphology (Fig. 1f). High-resolution TEM images displayed 2D-layered morphology, which was stacked on top of each other (Fig. 1g).

Redox-active behavior of TAPA-OPE was investigated by CV performed with respect to (w.r.t.) Ag/Ag^+ in acetonitrile and, two redox couple peaks were observed at 0.67/0.58 V and 0.02/-0.26 V (Fig. S8). This is a characteristic feature for the

ARTICLE

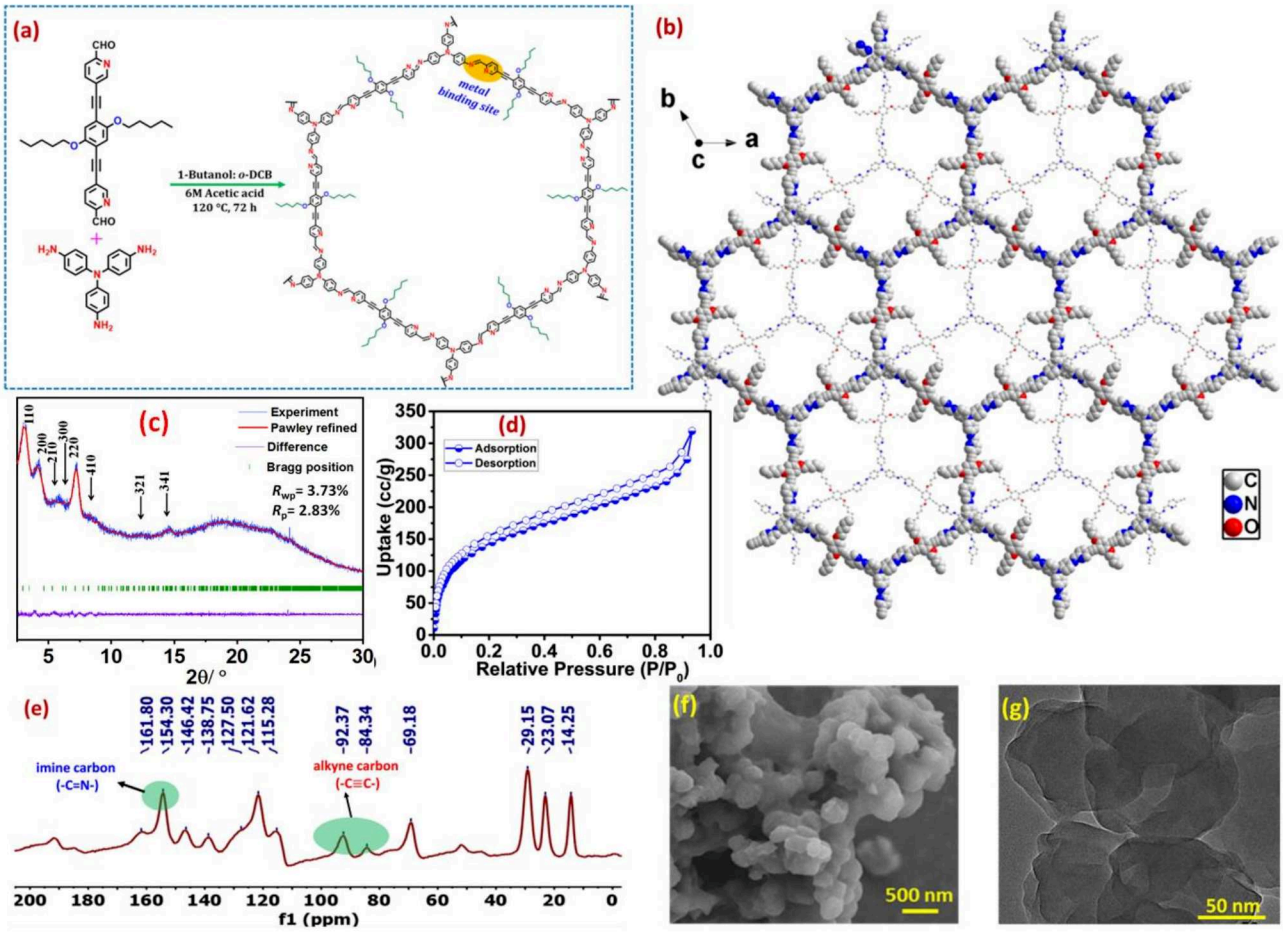

Fig. 1 (a) Synthetic scheme for TAPA-OPE COF. (b) Simulated structure of TAPA-OPE in staggered confirmation. Characterization of TAPA-OPE (c-g); (c) PXRD, (d) N_2 adsorption (77 K), (e) solid state ^{13}C NMR, (f) FE-SEM, and (g) TEM image.

formation of mono and bi-cationic species at the TAPA center, respectively, and is responsible for the redox-active nature of the COF.[44, 45]

The electrochemical bandgap for TAPA-OPE was calculated to be 3.17 eV. Further, owing to highly conjugated architecture, the electrical conductivity of TAPA-OPE was measured, which showed the value of 8.55 x 10^{-6} (±4) S cm^{-1}, illustrating the semiconducting nature of the COF material (Fig. S9).[46] Next, we envisioned the exploration of metal chelating ability of TAPA-OPE toward electroactive metal ion to realize COF-based single atom electrocatalysis. We have chosen the cobalt ion (Co^{2+}) due to its excellent electrocatalytic activity, high abundance, and significantly cheaper as compared to electroactive noble metals.[47] The detailed synthetic procedure for cobalt (Co^{2+}) complexation in the TAPA-OPE (Co-TAPA-OPE) is described in the experimental section (Fig. 2a). Co-TAPA-OPE was characterized by PXRD, FTIR, microscopic analysis (FESEM, TEM, HAADF-STEM, and elemental mapping), X-ray photoelectron spectroscopy (XPS), X-ray absorption near-edge structure (XANES) and extended X-ray absorption fine structure (EXAFS) studies. XPS analysis of Co-TAPA-OPE provided closer insight into the oxidation state of metal ions (Fig. 2b). Two intense peaks at 769.23 and 784.75 eV were attributed to the Co $^2p_{1/2}$ and Co $^2p_{3/2}$, respectively, confirming the presence of coordinated Co^{2+} metal ion.[34] Additionally, three peaks for carbon spectrum (C1s) at 284.79, 286.30, and 289.86 eV indicated the existence of three types of carbon and can be assigned for C-C, C=C/C=N, and C≡C, respectively. Two

ARTICLE

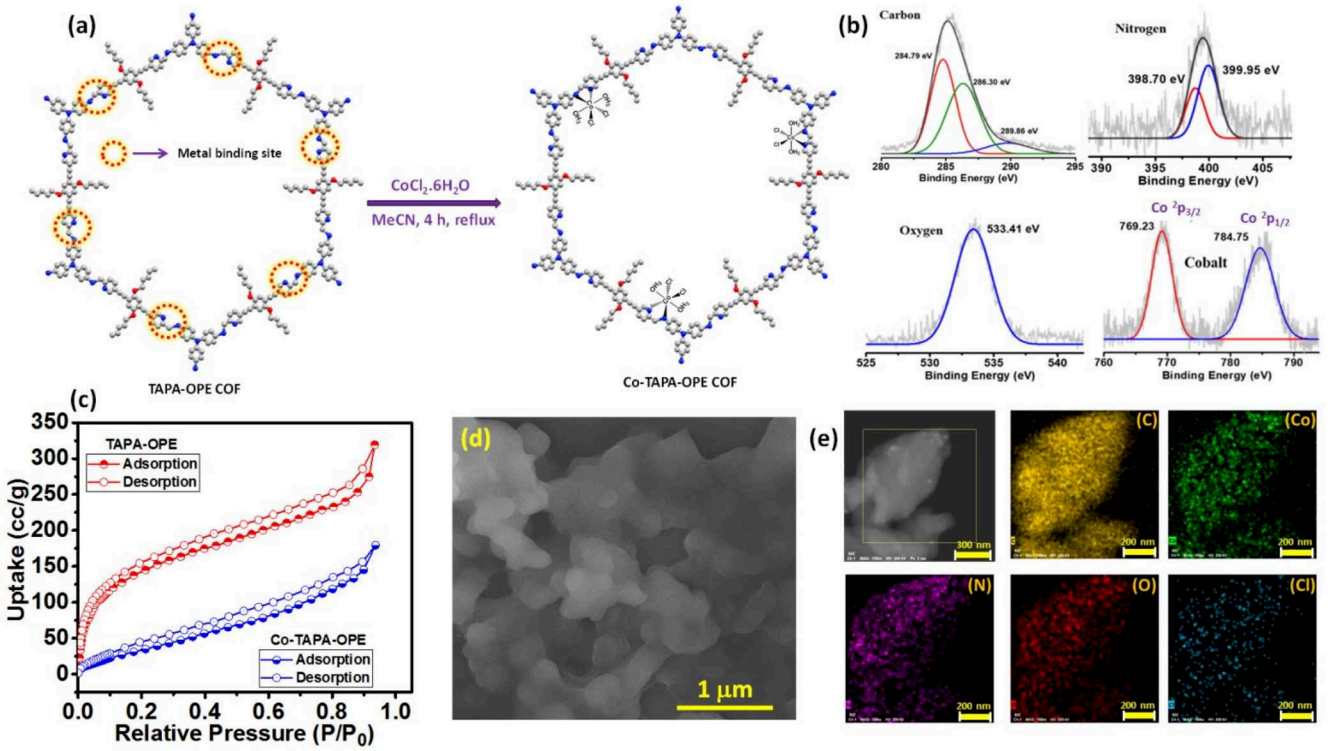

Fig. 2 (a) Synthesis of Co^{3+} metalated TAPA-OPE COF. (b-e) Characterization of Co-TAPA-OPE; (b) XPS spectra, (c) N_2 adsorption at 77 K, (d) FE-SEM, (e) a broad area HAADF-STEM image and the corresponding elemental maps in the region.

peaks for nitrogen at 398.70 and 399.95 eV could be attributed to the pyridinic and imino (-C=NH) nitrogen, respectively.[48] A peak at 533.41 eV corresponded to the oxygen atom that appeared for the alkoxy side-chain of OPE unit. The Inductive Coupled Plasma Atomic Emission Spectroscopy (ICP-AES) analysis indicated the presence of 2.8% cobalt in the Co-TAPA OPE. The attenuated total reflection (ATR)-FTIR spectra were recorded in the low-frequency region (150 cm^{-1} - 500 cm^{-1}) for both TAPA-OPE and Co-TAPA-OPE. The presence of the two characteristic bands at 278 cm^{-1} (Co-Cl) and 464 cm^{-1} (Co-N) in Co-TAPA-OPE indicated the covalent integration of Co^{2+} in the COF matrix (Fig. S10).[49] Next, the TGA-Mass spectrometry experiment performed for the Co-TAPA-OPE has shown good stability, and no weight loss was observed in the low-temperature region (<100 °C), supporting the absence of any guest molecule in the polymer matrix (Fig. S11a). Importantly, weight loss corresponding to the water molecule observed in the mass analysis corroborating the presence of water molecules in the coordination environment of the Co^{2+} (Fig. S11b). A similar PXRD pattern of the Co-TAPA-OPE was found as observed for the TAPA-OPE, illustrating the structural integrity was maintained after complexation with Co^{2+} (Fig. S12). Adsorption study of the Co- TAPA-OPE showed significantly decreased N_2 uptake at 77K (180 ml/g at 1 atm) as compared to the bare TAPA-OPE (320 ml/g at 1 atm), which could be attributed to the pore blocking after Co^{2+} coordination in the Co-TAPA-OPE (Fig. 2c). FE-SEM and TEM images of Co-TAPA-OPE displayed similar morphology to the bare TAPA-OPE (Fig. 2d-e, 3a), indicating that the COF's morphology remained intact after metalation. Further, the High-angle annular dark-field scanning transmission electron microscope (HAADF-STEM) image acquired for the Co-TAPA-OPE displayed bright intense spots at atomic scale, illustrating the presence of well-dispersed single metal atoms (Fig. 3b).[50-52] HAADF-STEM Energy-dispersive X-ray (EDX) analysis showed a homogeneous dispersion of cobalt (Co), chlorine (Cl), carbon (C), nitrogen (N) and oxygen (O) elements in the polymer matrix (Fig. 2e & S13). The loading amount of cobalt calculated by the EDX was found to be ~2.81 wt% (Fig. S13), which is in agreement with the ICP analysis.

ARTICLE

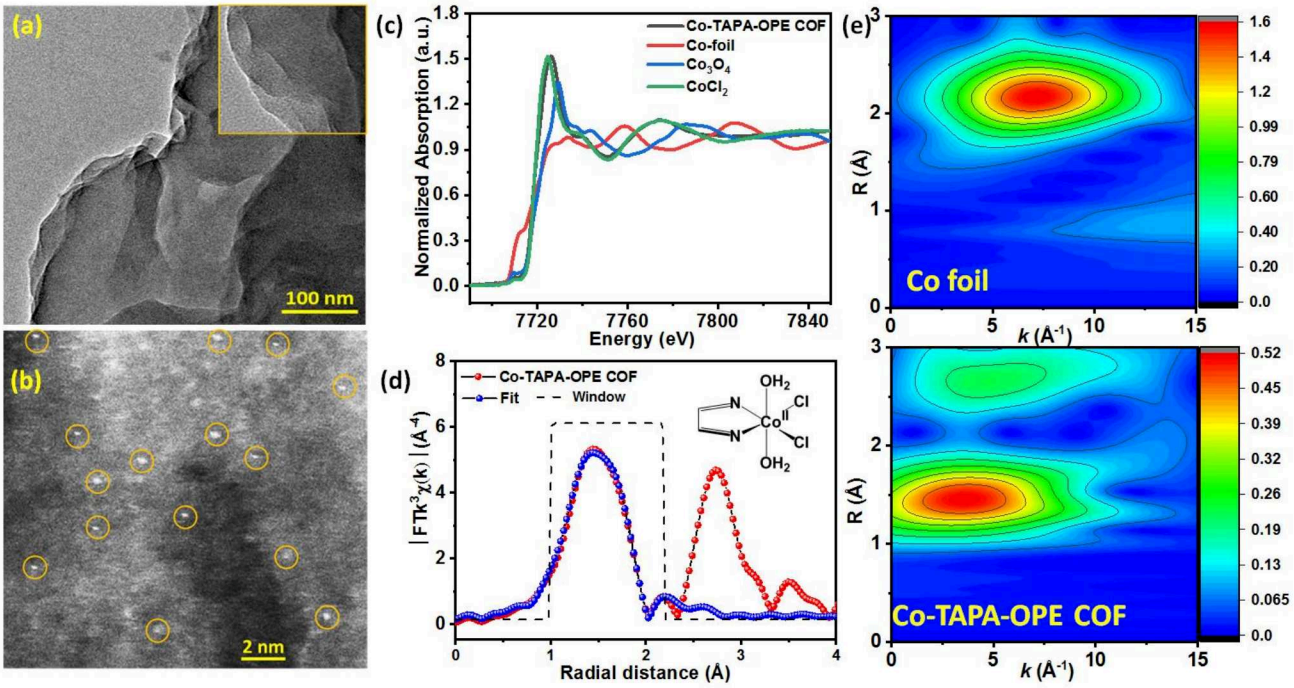

Fig. 3 (a) HRTEM image of Co-TAPA-OPE COF. (b) High resolution HAADF-STEM image. (c) XANES spectra at the Co K-edge of Co foil, $CoCl_2$, Co_3O_4, and Co-TAPA-OPE COF. (d) The corresponding EXAFS fitting curves of Co-TAPA-OPE COF at R space. (e) Wavelet transform (WT) for the EXAFS signals of Co foil, and Co-TAPA-OPE COF.

Next, X-ray absorption near-edge structure (XANES) and extended X-ray absorption fine structure (EXAFS) measurements were performed to elucidate the electronic structure and coordination environment of the Co-TAPA-OPE COF (Fig. 3c-e). As shown in Fig. 3c, the absorption edge position of Co-TAPA-OPE COF located near $CoCl_2$ rather than Co foil, suggesting that the Co in Co-TAPA-OPE COF carried a positive charge with the valence state of the Co being +2. More importantly, the Co K-edge absorption of Co-TAPA-OPE COF was close to $CoCl_2$, signifying the presence of atomically dispersed Co^{2+} ions.[53, 54]

Moreover, the EXAFS wavelet transform (WT) analysis was employed to discriminate the atomic configuration of Co-TAPA-OPE COF. The WT contour plots for Co foil showed the intensity maxima at 7.1 $Å^{-1}$ (Fig. 3e), which was subjected to the Co-Co coordination. In contrast, the WT contour plots for Co-TAPA-OPE COF exhibited an intensity maximum at 3.6 $Å^{-1}$, clearly ruled out the possibility of the presence of Co nanoparticles. Quantitative EXAFS fitting was performed at Co K-edge to extract the quantitative local structure parameters of Co atom in Co-TAPA-OPE COF (Fig. 3d, S14). The fitting curves based on a model structure of Co-TAPA-OPE COF demonstrated that the Co atom is coordinated in an octahedral geometry, carrying two Co-N bonds with a distance of 1.96 Å and two Co-Cl bonds in the equatorial plane with a distance of 2.16 Å (Table S1). Additionally, two H_2O molecules are coordinated in axial positions with a Co-O bond distance of 2.1 Å.[55]

Inspired by the unique structural features of Co-TAPA-OPE COF, the electrocatalytic activity was assessed toward CO_2 reduction in an H-type cell (Fig. 4a-h, S15). The electrocatalytic performance of the Co-TAPA-OPE towards CO_2RR was evaluated in 0.2 M $KHCO_3$ electrolyte solution by performing cyclic voltammetry, linear sweep voltammetry (LSV), and chronoamperometry study (Fig. 4a-c). LSV study was performed for Co-TAPA-OPE COF in the Ar- and CO_2-purged electrolytes (Fig. 4a). A noteworthy enhanced current density in CO_2 saturated solution over Ar-purged electrolyte is attributed to the direct CO_2RR through solvated CO_2. Cyclic voltammetry curve of Co-TAPA-OPE COF in Ar-saturated solution (pH-8.4) did not display any reduction peak in the region of negative potential. Whereas, the CO_2 saturated (pH-

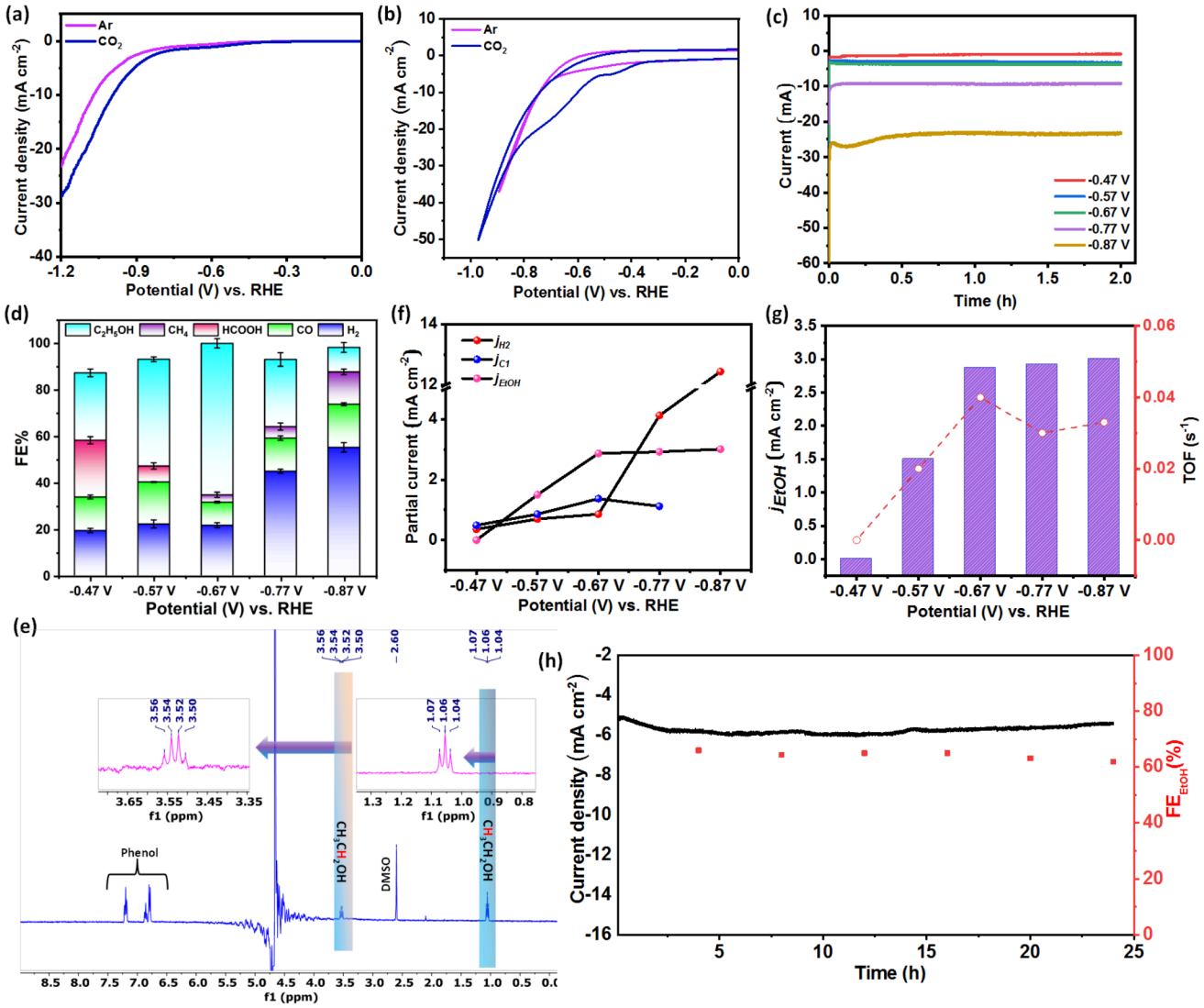

Fig. 4 (a) LSV plot showing the increased current density in presence of CO_2. (b) CV curve in Ar and CO_2 medium. (c) Current-time profile at different applied potential. (d) Product distribution plot during CO_2RR at different potentials. (e) ^{1}H NMR of electrolyte using solvent suppression method. (f) Plot showing partial current density at different potentials. (g) Partial current density plot of ethanol formation and corresponding TOF. (h) Long-term stability of the catalyst over 24 h at -0.67 V.

7.2) solution has exhibited a reduction peak at -0.4 V, which is accountable for the Co-catalyzed CO_2 reduction (Fig. 4b).[1] Controlled potential electrolysis (CPE) was performed for 2 h at -0.47, -0.57, -0.67, -0.77 and -0.87 V potentials (Fig. 4c). The chronoamperometry plot, as shown in Fig. 4c, showed a steady current at every individual potential from -0.47 to -0.87 V vs. RHE (Fig. 4c). The CO_2RR product distributions and subsequent Faradaic efficiency (FE) was examined as the function of applied potentials from −0.47 to −0.87 V over Co-TAPA-OPE COF (Fig. 4d, Table S2). The gaseous products and the liquid products were quantified using GC-MS and ^{1}H NMR, respectively (Fig. S16-17). NMR study confirmed the production of ethanol in the electrolyte along with the formation of a subtle amount of formate as liquid product in the course of CO_2RR (Fig. 4e). CO and CH_4 were detected as minor gaseous products. The ethanol production was not observed at the potential below -0.47 V and therefore, the

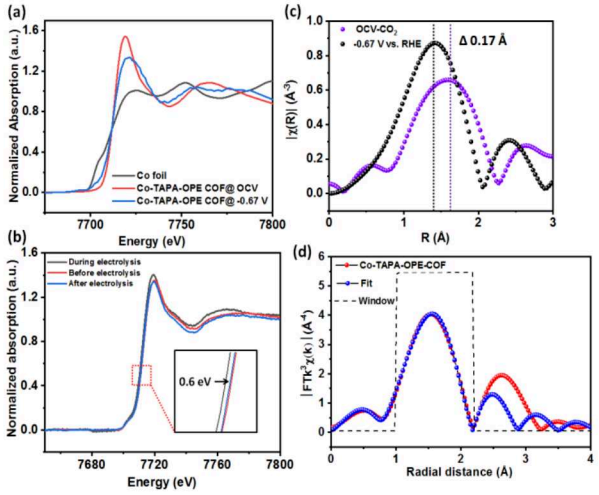

Fig. 5 (a) Normalized operando Co K-edge XANES spectra for Co-TAPA-OPE COF at various potentials (vs. RHE) in 0.2 M $KHCO_3$ aqueous solution which showed the change of oxidation state of Co. (b) Co K-edge XANES spectra for Co-TAPA-OPE COF before, during and after electrolysis. The inset shows the enlarged Co K-edge XANES spectra. (c) Fourier transformed magnitudes of EXAFS spectra (without phase correction) of Co-TAPA-OPE COF under open-circuit voltage bias in CO_3 and at −0.67 V (versus RHE). (d) EXAFS curve-fitting of Co-TAPA-OPE COF in R space after electrolysis at -0.67 V.

active potential for ethanol detection was found to be as low as -0.47 V. This observation suggests that the actual onset potential and overpotential are -0.47 V and 560 mV, respectively, considering the equilibrium potential of 0.09 V vs. RHE.[56] At -0.47 V, FE for ethanol formation was calculated to be 30.8%, which was significantly enhanced to ~ 66.8% at a potential of -0.67 V. To the best of our knowledge, this FE value of ~ 66.8% represents the highest FE for the electrocatalytic CO_2 to ethanol conversion among reported Co-based electrocatalysts (Table S3). In fact, the employment of single atom Co in a COF framework for ethanol formation is not reported to date (Table S4). The partial current density of ethanol was found to be 2.87 mA cm^{-2} at -0.67 V, which is quite significant in terms of electrochemical CO_2 reduction in H-type cell (Fig. 4f). After analyzing FE trends for each product, the intrinsic rate of CO_2-to-ethanol in terms of turnover frequency (TOF) was found to be 0.04 s^{-1} at -0.67 V (Fig. 4g). Flow cell was used to realize the mass transport limitation of CO_2, and it was observed that the partial current density of ethanol formation was increased significantly and maximum partial current was observed to be 35.8 mA cm^{-2} (Fig. S18). It was also observed that the H_2 generation was also suppressed at higher overpotentials. The source of carbonaceous products was confirmed by performing electrolysis using isotopic CO_2 ($^{13}CO_2$) in 0.2 M Na_2SO_4 solution. The extracted ^{1}H-NMR from the electrolyte evidently showed a split triplet peak due to coupling with ^{13}C of ethanol at 1.05 ppm, which corroborated the origin of ethanol from the electroreduction of CO_2 (Fig. S19).[13] Additionally, GC-MS study of the electrolyte solution after electrolysis using $^{13}CO_2$ as reactant showed the presence of a peak at m/z = 32 for $[^{13}CH_2OH]^+$ formation instead m/z at 31 for $[CH_2OH]^+$ (Fig. S20). The chronoamperometry study with the catalyst was performed over a 24 h span at -0.67 V, showing excellent stability with respect to both current density and FE of CO_2-to-ethanol (Fig. 4h). Furthermore, the electrochemical double layer capacitance (C_{dl}), which is directly related to electrochemically active surface area (ECSA), was found to be similar before and after chronoamperometry measurement at different potentials (Fig. S21).[16] We noticed that the FE and CO_2RR product distributions varied at the different applied potential. The total current density represents the overall conversion of CO_2 to all products. The charge transfer resistance (R_{ct}) was realized by measuring impedance in Ar and CO_2-purged solutions and it was noticed that CO_2-purged solution exhibited lower R_{ct} at -0.67 V (Fig. S22). The kinetics of ethanol formation was realized using Tafel plot. The Tafel slope was calculated to be 215.7 mV dec^{-1} (Fig. S23). The morphology of Co-OPE-TAPA COF was assessed using FESEM after electrolysis at -0.67 V for 2 h, and it showed no noticeable change in morphology after electrochemical CO_2RR (Fig. S24). Further, the CO_2RR activity was also evaluated for metal-free TAPA-OPE COF. However, LSV curve of the TAPA-OPE COF showed no significant enhancement in the current density either in Ar atmosphere or in CO_2 atmosphere (Fig. S25). Furthermore, we also executed chronoamperometry in the range of -0.3 V to -0.9 V for the TAPA-OPE COF. Subsequently, the CO_2RR product was analyzed by GC-MS for gaseous products and ^{1}H-NMR for liquid products (Fig. S26-S27).

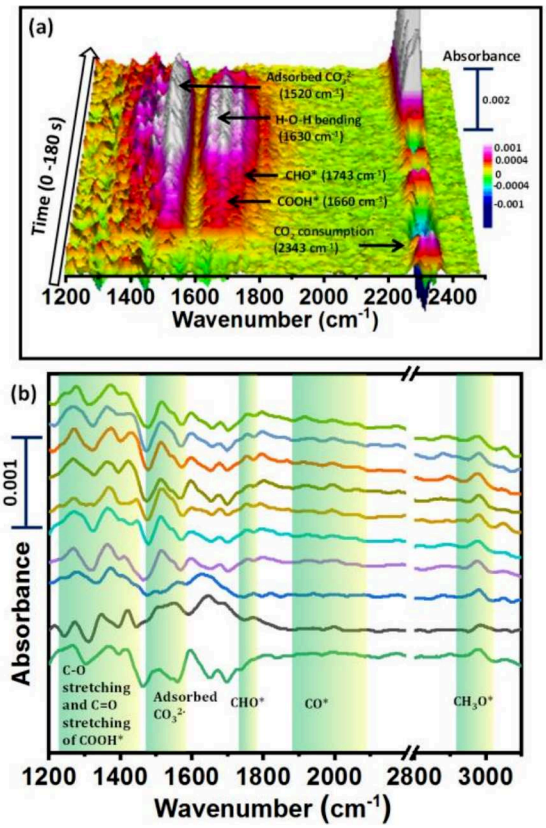

Fig. 6 *In-situ* FTIR study of electrochemical CO_2RR with Co-TAPA-OPE. (a) Rapid scan measurement during LSV at 10 mV s^{-1}. (b) *In-situ* FTIR study during controlled potential electrolysis at -0.67 V.

Nonetheless, hydrogen was the only product obtained from the proton reduction, and no liquid or gaseous carbonaceous product was observed, which unambiguously confirmed that the Co is the active catalytic center for electrocatalytic CO_2 reduction.

Additionally, electrochemical CO_2RR was performed at four different pH of 6.8, 7.2, 7.8 and 8.5 to examine the correlation of onset potential with pH.[57-59] In LSV curves, the overpotential at pH 6.8, 7.2, 7.8 and 8.5 are found to be 659, 415, 516, 687 mV, respectively, at 1 mA cm^2. This observation suggests that the overpotential value differs with the pH of electrolyte. Additionally, the FE% of the Co-TAPA-OPE COF varied with the pH of the electrolyte which was observed by performing electrolysis at different potential (-0.6, -0.7, -0.8, -0.9 and -1 V) at different pH (Fig. S28).

In-situ XAS measurements were performed to gain insight of the oxidation state and coordination environment of single Co site on Co-TAPA-OPE COF, (Fig. S29). Fig. 5a and, 5b display the normalized operando Co K-edge XANES spectra which showed the shift of the Co K-edge to ~0.6 eV lower energy during electrolysis at -0.67 V vs. RHE (Fig. 5b inset). This suggested the change in oxidation state of Co^{2+} towards lower oxidation state.[60] Average oxidation state of the Co site was estimated by developing correlation diagram of known Co-samples using the energy position at half of the edge step. When the potential of -0.67 V was applied, an average oxidation state of 1.72 was observed, indicating that partial reduction of Co^{2+} to $Co^{+2-\delta}$ ($0<\delta<1$) (Fig. S30).[61] After electrochemical CO_2 reduction, the Co K-edge of Co-TAPA-OPE COF shifted back to higher energy, which indicates the recovery of +2 oxidation-state of Co after CO_2 reduction (Fig. 5b). The peak contributing Co-O, Co-N signature at approximately 1.58 Å in the Fourier transform of the EXAFS spectrum decreased slightly during electrolysis. This indicates the change of the coordination environment in Co single site during CO_2RR because of the strong binding of the CO_2 (Fig. 5c). The peak shifted (~ 0.17 Å) to shorter lengths during CO_2 reduction with the catalyst biased at -0.67 V vs. RHE, compared with that under open-circuit voltage.

In addition, quantitative EXAFS fitting was performed at Co K-edge to extract the quantitative local structure parameters of Co atom in Co-TAPA-OPE COF after electrolysis at -0.67 V (Fig. S31). The fitting curves demonstrated octahedral geometry of the isolated Co atom with two Co-N bonds, two Co-Cl bonds in the equatorial plane and two coordinated H_2O molecules in axial positions (Table S3). Both XANES and EXAFS data supports the stability of Co-TAPA-OPE COF during electrolysis as it is important to understand the structural evolution of the material during electroreduction.[62, 63]

In-situ FTIR measurement using external reflection configuration was implemented to identify the product formation pathway (Fig. 6). A Si prism was used beveled at 60°. A detailed description of the setup is given in the supporting information (Fig. S32). The spectra collected at different potential in Ar atmosphere were used as background to minimize the effect of proton reduction pathway. Then, CO_2 was passed as feeding gas to perform controlled potential electrolysis (CPE). The rapid scan was performed using synchronization technique to achieve the large number of spectra in single pulse for 180 s during LSV measurement under CO_2 atmosphere. During LSV measurement, *in-situ* IR experiment was performed and spectra were collected in a regular time interval. A peak at 1660 cm^{-1} corresponded to C=O stretching of COOH* species.[64] Furthermore, a band at around 1752 cm^{-1} could be ascribed as surface bound CHO* species which is a key intermediate for C-C coupling (Fig. 6a).[18, 65] Next, FTIR spectra were taken during chronoamperometric study at the applied potential of -0.67 V vs. RHE to observe intermediate species during CO_2 electroreduction (Fig. 6b). The peak appeared at 1520 cm^{-1} was corresponded to the carbonate (CO_3^{2-}) species. The peaks observed during electrolysis at 1260, and 1380 cm^{-1} corresponded to C-OH stretching (O-H deformation) and C-O stretching of COOH* species, respectively, which is the most important intermediate in the course of formation of CO.[64] Apparently, we observed surface adsorbed asymmetric IR band of CO at 1902, and 1996 cm^{-1}. Further, a band displayed at 1752 cm^{-1} could be attributed to the CHO* species which is likely to be the key intermediate for C-C coupling.[66] Meanwhile, the formation of another important intermediate CH_3O* was observed at 2960 cm^{-1} during chronoamperometric study at -0.67 V vs. RHE.[67, 68]

Density functional theory (DFT) calculation was performed in line of EXAFS and *in-situ* IR analysis to deduce the plausible mechanism of electrocatalytic CO_2 reduction to ethanol in Co^{2+} metalated COF which is aptly supported by relative Gibbs free energy (ΔG) plot (Fig. 7, S33-S35).[14, 16, 20, 22, 69-71] In brief, the EXAFS study suggested hexa-coordinated environment around the Co^{2+}, coordinated with two water molecules (axial positions), two chloride ion and two nitrogen atom of the COF framework (Fig. 3d). Similar hexa-coordinated environment around Co^{2+} has taken into consideration for DFT calculations with smallest repetitive unit of the framework consisting of one OPE and one TAPA unit, named as $[Co^{II}(\eta^2\text{-COF-N,N'})(H_2O)_2Cl_2]$ **(H_2O*OH_2)** (Fig. 7, S33). The catalysis initiated possibly with simultaneous CO_2-binding with proton-coupled reduction of $[Co^{II}(\eta^2\text{-COF-N,N'})(H_2O)_2Cl_2]$ **(H_2O*OH_2)** to form $[Co^{II}(\eta^2\text{-COF-N,N'})(COOH)(H_2O)Cl_2]$ **$(H_2O*COOH)$** through removal of one loosely bound axial water molecule (ΔG = +1.07 eV).[20, 69, 70, 72, 73] Next, another simultaneous CO_2-binding with proton-coupled reduction of $[Co^{II}(\eta^2\text{-COF-N,N'})(COOH)(H_2O)Cl_2]$ **$(H_2O*COOH)$** likely to be occurred by releasing the remaining water molecule to generate intermediate $[Co^{II}(\eta^2\text{-COF-N,N'})(COOH)_2Cl_2]$ **(HOOC*COOH)**, which was found to be the most uphill process of the whole catalytic mechanism (ΔG = +2.25 eV).

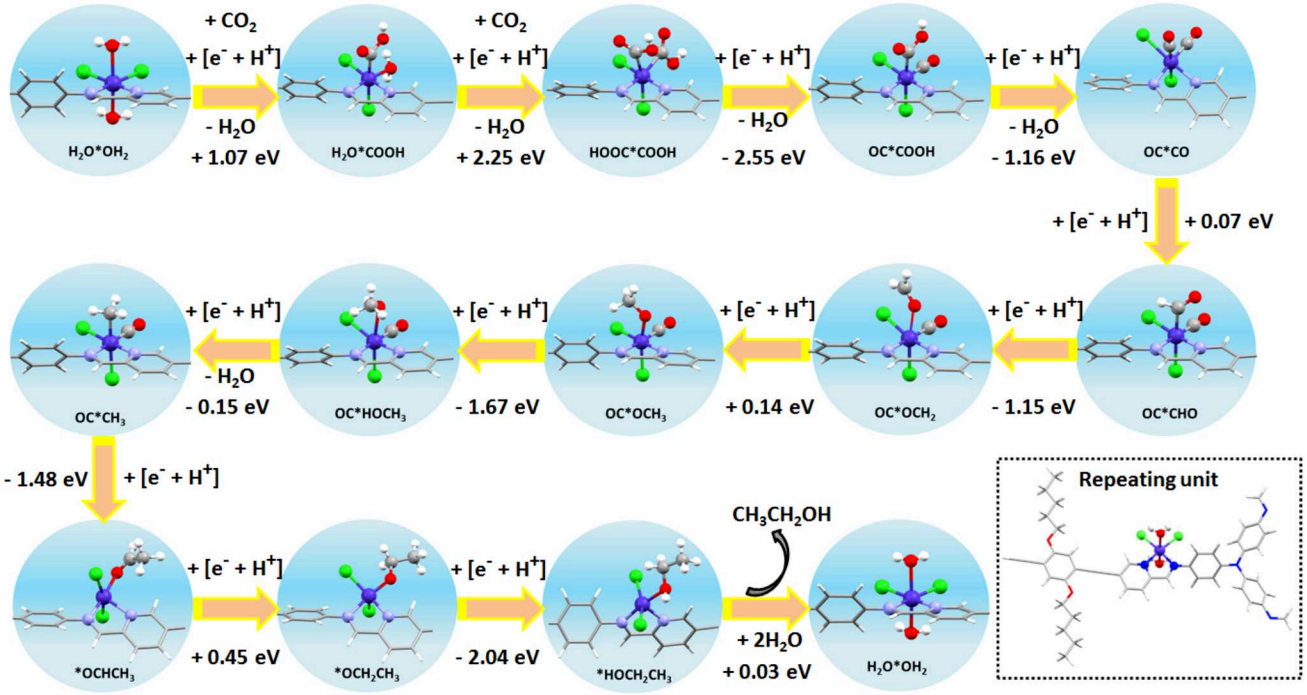

Fig. 7. Possible mechanism for electrocatalytic CO_2 to CH_3CH_2OH reduction on Co^{3+} metalated COF with corresponding Gibbs free energy change (ΔG) values computed by DFT, at an applied potential of -0.67 V vs. RHE.

In the following steps, proton-coupled reduction followed by water elimination from the intermediate [Co^{II}(η^2-COF-N,N′)$(COOH)_2Cl_2$] **(HOOC*COOH)** would afford [Co^{II}(η^2-COF-N,N′)(COOH)$(CO)Cl_2$] **(OC*COOH)** (ΔG = -2.55 eV), which upon further proton-coupled reduction and simultaneous water elimination would lead to the formation of [Co^{II}(η^2-COF-N,N′)$(CO)_2Cl_2$] **(OC*CO)** (ΔG = -1.16 eV). Next proton-coupled reduction would result in the reduction of axial CO of [Co^{II}(η^2-COF-N,N′)$(CO)_2Cl_2$] **(OC*CO)** to afford [Co^{II}(η^2-COF-N,N′)(CHO)$(CO)Cl_2$] **(OC*CHO)** (ΔG = +0.07 eV).[20] The subsequent proton-coupled reduction would convert the intermediate [Co^{II}(η^2-COF-N,N′)(CHO)$(CO)Cl_2$] **(OC*CHO)** to [Co^{II}(η^2-COF-N,N′)$(OCH_2)(CO)Cl_2$] **($OC*OCH_2$)** (ΔG = -1.15 eV) to [Co^{II}(η^2-COF-N,N′)$(OCH_3)(CO)Cl_2$] **($OC*OCH_3$)** (ΔG = +0.14 eV) to [Co^{II}(η^2-COF-N,N′)$(HOCH_3)(CO)Cl_2$] **($OC*HOCH_3$)** (ΔG = -1.67 eV), which after proton-coupled reduction and subsequent water elimination would afford [Co^{II}(η^2-COF-N,N′)$(CH_3)(CO)Cl_2$] **($OC*CH_3$)** (ΔG = -0.15 eV). Interestingly, upon proton-coupled reduction of [Co^{II}(η^2-COF-N,N′)$(CH_3)(CO)Cl_2$] **($OC*CH_3$)**, a rapid C-C coupling is likely to be occurred to generate C_2-intermediate [Co^{II}(η^2-COF-N,N′)$(OCHCH_3)Cl_2$] **($*OCHCH_3$)** (ΔG = -1.48 eV). In the next step, proton-coupled reduction of [Co^{II}(η^2-COF-N,N′)$(OCHCH_3)Cl_2$] **($*OCHCH_3$)** would afford [Co^{II}(η^2-COF-N,N′)$(OCH_2CH_3)Cl_2$] **($*OCH_2CH_3$)** (ΔG = +0.45 eV), which upon further proton-coupled reduction resulted in the formation of [Co^{II}(η^2-COF-N,N′)$(HOCH_2CH_3)Cl_2$] **($*HOCH_2CH_3$)** (ΔG = -2.04 eV). Lastly, the intermediate [Co^{II}(η^2-COF-N,N′)$(HOCH_2CH_3)Cl_2$] **($*HOCH_2CH_3$)** expected to release ethanol (ΔG = +0.03 eV) and the initial catalyst [Co^{II}(η^2-COF-N,N′)$(H_2O)_2Cl_2$] **(H_2O*OH_2)** would be regenerated by retaking two water molecules, which would then re-enter into the catalytic cycle to continuing the ethanol production (Fig. 7, S34-S35).

Conclusions

In conclusion, we have synthesized donor-acceptor based electroactive COF material (TAPA-OPE), which possessed metal-chelating sites and, therefore, utilized further for coordinately grafting of the Co^{2+} upon post-synthetic modification to realize single atom driven COF based electrocatalyst (Co-TAPA-OPE) for selective reduction of the CO_2 to ethanol. The XANES and EXAFS analysis ensured the octahedral geometry of the atomically dispersed Co^{2+} in the Co-TAPA-OPE. The electrochemical CO_2 reduction to ethanol using Co-TAPA-OPE was achieved with the active potential of -0.47 V. The maximum partial current density of -2.87 mA cm^{-2} and maximum FE of ~ 66.8% was achieved during the CO_2RR. The chronoamperometry experiment was performed over a period of 24 h and activity was found to be retained, indicating impressive catalytic stability. *In-situ* XAS study demonstrated the reversible change in the oxidation state of Co^{2+} single atom site. It also provided the support of stability of the catalyst after electrolysis. Further, *In-situ* FTIR study executed to monitor the real time reaction progress which has provided experimental evidence about the intermediates formed during the CO_2RR. Further, based on the experimental results, a plausible mechanism for the CO_2 reduction to ethanol was elucidated through the DFT calculation. Thus, the present work demonstrates a sustainable approach towards developing COF based single atom driven electrocatalyst for the electrochemical CO_2 reduction to value added fuels. This study

could pave a way towards developing COF based cheap and stable electrode materials for utilizing CO_2 to valuable C_2-feedstocks and achieving carbon neutrality.

Acknowledgements

TKM gratefully acknowledges the SERB, Department of Science and Technology (DST), Govt. of India, Project no. - CRG/2019/005951 and Project No. - SPR/2021/000592, under SUPRA scheme, for financial support. TKM and AS is grateful to the SERB, DST, Government of India, RAK-CAM (from UAE), SSL, ICMS, and JNCASR for financial support. SAMat research facility, Sheikh Saqr senior fellowship (TKM) is also gratefully acknowledged. SB acknowledges JNCASR for the support and DST for the fellowship and funding. FAR is thankful to the CSIR, Government of India for the fellowship. We thank Dr. W. A. Caliebe for assistance in EXAFS measurement at PETRA III of DESY, Helmholtz Association (HGF), (beamline P64) supported by the DST. The support and the resources provided by "PARAM Yukti Facility" under the National Supercomputing Mission, Government of India, at the Jawaharlal Nehru Centre for Advanced Scientific Research are gratefully acknowledged. Authors thank Mr. Arindam Ghosh for the initial XAS measurement. Authors thank Dr. Abdul Ahad for helping to analyze XAS results.

Author Contributions

# Ashish Singh and Soumitra Barman contributed equally.

Conflicts of interest

There are no conflicts to declare.

References

1. J. Yin, Z. Yin, J. Jin, M. Sun, B. Huang, H. Lin, Z. Ma, M. Muzzio, M. Shen, C. Yu, H. Zhang, Y. Peng, P. Xi, C.-H. Yan and S. Sun, *J. Am. Chem. Soc.*, 2021, **143**, 15335-15343.
2. H. Wang, Y.-K. Tzeng, Y. Ji, Y. Li, J. Li, X. Zheng, A. Yang, Y. Liu, Y. Gong, L. Cai, Y. Li, X. Zhang, W. Chen, B. Liu, H. Lu, N. A. Melosh, Z.-X. Shen, K. Chan, T. Tan, S. Chu and Y. Cui, *Nat. Nanotechnol.*, 2020, **15**, 131-137.
3. L. Ji, L. Li, X. Ji, Y. Zhang, S. Mou, T. Wu, Q. Liu, B. Li, X. Zhu, Y. Luo, X. Shi, A. M. Asiri and X. Sun, *Angew. Chem. Int. Ed.*, 2020, **59**, 758-762.
4. C. W. Li, J. Ciston and M. W. Kanan, *Nature*, 2014, **508**, 504-507.
5. C. Costentin, M. Robert and J.-M. Savéant, *Chem. Soc. Rev.*, 2013, **42**, 2423-2436.
6. S. Karmakar, S. Barman, F. A. Rahimi and T. K. Maji, *Energy Environ. Sci.*, 2021, **14**, 2429-2440.
7. P. Verma, A. Singh, F. A. Rahimi, P. Sarkar, S. Nath, S. K. Pati and T. K. Maji, *Nat. commun.*, 2021, **12**, 1-14.
8. P. Verma, F. A. Rahimi, D. Samanta, A. Kundu, J. Dasgupta and T. K. Maji, *Angew. Chem. Int. Ed.*, 2022, **61**, e202116094.
9. S. Barman, A. Singh, F. A. Rahimi and T. K. Maji, *J. Am. Chem. Soc.*, 2021, **143**, 16284-16292.
10. Y. Liu, Y. Zhang, K. Cheng, X. Quan, X. Fan, Y. Su, S. Chen, H. Zhao, Y. Zhang, H. Yu and M. R. Hoffmann, *Angew. Chem. Int. Ed.*, 2017, **56**, 15607-15611.
11. Y. Yang, Y. Yang, Y. Liu, S. Zhao and Z. Tang, *Small Sci.*, 2021, **1**, 2100015.
12. S. Lee, G. Park and J. Lee, *ACS Catal.*, 2017, **7**, 8594-8604.
13. J. Du, S. Li, S. Liu, Y. Xin, B. Chen, H. Liu and B. Han, *Chem. Sci.*, 2020, **11**, 5098-5104.
14. T. N. Nguyen, J. Guo, A. Sachindran, F. Li, A. Seifitokaldani and C.-T. Dinh, *J. Mater. Chem. A*, 2021, **9**, 12474-12494.
15. Y. Liu, X. Fan, A. Nayak, Y. Wang, B. Shan, X. Quan and T. J. Meyer, *Proc. Natl. Acad. Sci.*, 2019, **116**, 26353-26358.
16. H. Xu, D. Rebollar, H. He, L. Chong, Y. Liu, C. Liu, C.-J. Sun, T. Li, J. V. Muntean and R. E. Winans, *Nat. Energy*, 2020, **5**, 623-632.
17. Y. Zhou, F. Che, M. Liu, C. Zou, Z. Liang, P. De Luna, H. Yuan, J. Li, Z. Wang, H. Xie, H. Li, P. Chen, E. Bladt, R. Quintero-Bermudez, T.-K. Sham, S. Bals, J. Hofkens, D. Sinton, G. Chen and E. H. Sargent, *Nat. Chem.*, 2018, **10**, 974-980.
18. K. Jiang, R. B. Sandberg, A. J. Akey, X. Liu, D. C. Bell, J. K. Nørskov, K. Chan and H. Wang, *Nat. Catal.*, 2018, **1**, 111-119.
19. F. Li, Y. C. Li, Z. Wang, J. Li, D.-H. Nam, Y. Lum, M. Luo, X. Wang, A. Ozden, S.-F. Hung, B. Chen, Y. Wang, J. Wicks, Y. Xu, Y. Li, C. M. Gabardo, C.-T. Dinh, Y. Wang, T.-T. Zhuang, D. Sinton and E. H. Sargent, *Nat. Catal.*, 2020, **3**, 75-82.
20. S. Gonglach, S. Paul, M. Haas, F. Pillwein, S. S. Sreejith, S. Barman, R. De, S. Müllegger, P. Gerschel, U.-P. Apfel, H. Coskun, A. Aljabour, P. Stadler, W. Schöfberger and S. Roy, *Nat. Commun.*, 2019, **10**, 3864.
21. Y. Zhang, K. Li, M. Chen, J. Wang, J. Liu and Y. Zhang, *ACS Appl. Nano Mater.*, 2020, **3**, 257-263.
22. D. Karapinar, C. E. Creissen, J. G. Rivera de la Cruz, M. W. Schreiber and M. Fontecave, *ACS Energy Lett.*, 2021, **6**, 694-706.
23. X. Lv, L. Shang, S. Zhou, S. Li, Y. Wang, Z. Wang, T.-K. Sham, C. Peng and G. Zheng, *Adv. Energy Mater.*, 2020, **10**, 2001987.
24. D. Karapinar, N. T. Huan, N. Ranjbar Sahraie, J. Li, D. Wakerley, N. Touati, S. Zanna, D. Taverna, L. H. Galvão Tizei, A. Zitolo, F. Jaouen, V. Mougel and M. Fontecave, *Angew. Chem. Int. Ed.*, 2019, **58**, 15098-15103.
25. N.-T. Suen, Z.-R. Kong, C.-S. Hsu, H.-C. Chen, C.-W. Tung, Y.-R. Lu, C.-L. Dong, C.-C. Shen, J.-C. Chung and H. M. Chen, *ACS Catalysis*, 2019, **9**, 5217-5222.
26. K. Lv, Y. Fan, Y. Zhu, Y. Yuan, J. Wang and Q. Zhang, *J. Mater. Chem. A*, 2018, **6**, 5025-5031.
27. Z.-Q. Liang, T.-T. Zhuang, A. Seifitokaldani, J. Li, C.-W. Huang, C.-S. Tan, Y. Li, P. De Luna, C. T. Dinh and Y. Hu, *Nat. Commun.*, 2018, **9**, 1-8.
28. D. Karapinar, N. T. Huan, N. Ranjbar Sahraie, J. Li, D. Wakerley, N. Touati, S. Zanna, D. Taverna, L. H. Galvão Tizei and A. Zitolo, *Angew. Chem. Int. Ed.*, 2019, **58**, 15098-15103.
29. P. Iyengar, M. J. Kolb, J. Pankhurst, F. Calle-Vallejo and R. Buonsanti, *ACS Catal.*, 2021, **11**, 13330-13336.
30. C. S. Diercks and O. M. Yaghi, *Science*, 2017, **355**, eaal1585.
31. K. Geng, T. He, R. Liu, S. Dalapati, K. T. Tan, Z. Li, S. Tao, Y. Gong, Q. Jiang and D. Jiang, *Chem. Rev.*, 2020, **120**, 8814-8933.

32. R.-B. Lin and B. Chen, *Joule*, 2018, **2**, 1030-1032.
33. M. Lu, M. Zhang, J. Liu, Y. Chen, J. P. Liao, M. Y. Yang, Y. P. Cai, S. L. Li and Y. Q. Lan, *Angew. Chem. Int. Ed.*, 2022, **61**, e202200003.
34. C. Li, W. Ju, S. Vijay, J. Timoshenko, K. Mou, D. A. Cullen, J. Yang, X. Wang, P. Pachfule and S. Brückner, *Angew. Chem. Int. Ed.*, 2022, **134**, e202114707.
35. B. Han, X. Ding, B. Yu, H. Wu, W. Zhou, W. Liu, C. Wei, B. Chen, D. Qi, H. Wang, K. Wang, Y. Chen, B. Chen and J. Jiang, *J. Am. Chem. Soc.*, 2021, **143**, 7104-7113.
36. H. B. Yang, S.-F. Hung, S. Liu, K. Yuan, S. Miao, L. Zhang, X. Huang, H.-Y. Wang, W. Cai, R. Chen, J. Gao, X. Yang, W. Chen, Y. Huang, H. M. Chen, C. M. Li, T. Zhang and B. Liu, *Nat. Energy*, 2018, **3**, 140-147.
37. J. Han, P. An, S. Liu, X. Zhang, D. Wang, Y. Yuan, J. Guo, X. Qiu, K. Hou and L. Shi, *Angew. Chem. Int. Ed.*, 2019, **58**, 12711-12716.
38. M. Li, H. Wang, W. Luo, P. C. Sherrell, J. Chen and J. Yang, *Adv. Mater.*, 2020, **32**, 2001848.
39. Y. Yang, Y. Yang, Z. Pei, K.-H. Wu, C. Tan, H. Wang, L. Wei, A. Mahmood, C. Yan and J. Dong, *Matter*, 2020, **3**, 1442-1476.
40. G. Lin, H. Ding, D. Yuan, B. Wang and C. Wang, *J. Am. Chem. Soc.*, 2016, **138**, 3302-3305.
41. F. Auras, L. Ascherl, A. H. Hakimioun, J. T. Margraf, F. C. Hanusch, S. Reuter, D. Bessinger, M. Döblinger, C. Hettstedt and K. Karaghiosoff, *J. Am. Chem. Soc.*, 2016, **138**, 16703-16710.
42. A. Singh, S. Roy, C. Das, D. Samanta and T. K. Maji, *Chem. Commun.*, 2018, **54**, 4465-4468.
43. M. Lu, M. Zhang, C. G. Liu, J. Liu, L. J. Shang, M. Wang, J. N. Chang, S. L. Li and Y. Q. Lan, *Angew. Chem.*, 2021, **133**, 4914-4921.
44. P. Blanchard, C. Malacrida, C. Cabanetos, J. Roncali and S. Ludwigs, *Polym. Int.*, 2019, **68**, 589-606.
45. A. Singh, D. Samanta and T. K. Maji, *ChemElectroChem*, 2019, **6**, 3756-3763.
46. C. R. Mulzer, L. Shen, R. P. Bisbey, J. R. McKone, N. Zhang, H. c. D. Abruña and W. R. Dichtel, *ACS Cent. Sci.*, 2016, **2**, 667-673.
47. C. Li, X. Tong, P. Yu, W. Du, J. Wu, H. Rao and Z. M. Wang, *J. Mater. Chem. A*, 2019, **7**, 16622-16642.
48. A. M. Khattak, Z. A. Ghazi, B. Liang, N. A. Khan, A. Iqbal, L. Li and Z. Tang, *J. Mater. Chem. A*, 2016, **4**, 16312-16317.
49. G. W. Watt and D. S. Klett, *Inorg. Chem.*, 1964, **3**, 782-783.
50. W. Wan, C. A. Triana, J. Lan, J. Li, C. S. Allen, Y. Zhao, M. Iannuzzi and G. R. Patzke, *ACS Nano*, 2020, **14**, 13279-13293.
51. M. Zhang, Y.-G. Wang, W. Chen, J. Dong, L. Zheng, J. Luo, J. Wan, S. Tian, W.-C. Cheong and D. Wang, *J. Am. Chem. Soc.*, 2017, **139**, 10976-10979.
52. L. Yang, L. Shi, D. Wang, Y. Lv and D. Cao, *Nano Energy*, 2018, **50**, 691-698.
53. J. Di, C. Chen, S.-Z. Yang, S. Chen, M. Duan, J. Xiong, C. Zhu, R. Long, W. Hao, Z. Chi, H. Chen, Y.-X. Weng, J. Xia, L. Song, S. Li, H. Li and Z. Liu, *Nat. Commun.*, 2019, **10**, 2840.
54. T. Sun, S. Zhao, W. Chen, D. Zhai, J. Dong, Y. Wang, S. Zhang, A. Han, L. Gu, R. Yu, X. Wen, H. Ren, L. Xu, C. Chen, Q. Peng, D. Wang and Y. Li, *Proc. Natl. Acad. Sci.*, 2018, **115**, 12692-12697.
55. L. Cao, Q. Luo, W. Liu, Y. Lin, X. Liu, Y. Cao, W. Zhang, Y. Wu, J. Yang, T. Yao and S. Wei, *Nat. Catal.*, 2019, **2**, 134-141.
56. S. Nitopi, E. Bertheussen, S. B. Scott, X. Liu, A. K. Engstfeld, S. Horch, B. Seger, I. E. Stephens, K. Chan and C. Hahn, *Chem. Rev.*, 2019, **119**, 7610-7672.
57. Y. Y. Birdja, E. Pérez-Gallent, M. C. Figueiredo, A. J. Göttle, F. Calle-Vallejo and M. T. Koper, *Nat. Energy*, 2019, **4**, 732-745.
58. S. Bhunia, K. Bhunia, B. C. Patra, S. K. Das, D. Pradhan, A. Bhaumik, A. Pradhan and S. Bhattacharya, *ACS Appl. Mater. Interfaces*, 2018, **11**, 1520-1528.
59. H.-J. Zhu, M. Lu, Y.-R. Wang, S.-J. Yao, M. Zhang, Y.-H. Kan, J. Liu, Y. Chen, S.-L. Li and Y.-Q. Lan, *Nat. Commun.*, 2020, **11**, 497.
60. H. B. Yang, S.-F. Hung, S. Liu, K. Yuan, S. Miao, L. Zhang, X. Huang, H.-Y. Wang, W. Cai and R. Chen, *Nat. Energy*, 2018, **3**, 140-147.
61. J. Han, P. An, S. Liu, X. Zhang, D. Wang, Y. Yuan, J. Guo, X. Qiu, K. Hou, L. Shi, Y. Zhang, S. Zhao, C. Long and Z. Tang, *Angew. Chem. Int. Ed.*, 2019, **58**, 12711-12716.
62. S. Zhao, C. Tan, C.-T. He, P. An, F. Xie, S. Jiang, Y. Zhu, K.-H. Wu, B. Zhang and H. Li, *Nat. Energy*, 2020, **5**, 881-890.
63. S. Zhao, Y. Yang and Z. Tang, *Angew. Chem. Int. Ed.*, 2022, **61**, e202110186.
64. N. J. Firet and W. A. Smith, *ACS Catal.*, 2017, **7**, 606-612.
65. A. Wuttig, C. Liu, Q. Peng, M. Yaguchi, C. H. Hendon, K. Motobayashi, S. Ye, M. Osawa and Y. Surendranath, *ACS Cent. Sci.*, 2016, **2**, 522-528.
66. W. Ma, S. Xie, T. Liu, Q. Fan, J. Ye, F. Sun, Z. Jiang, Q. Zhang, J. Cheng and Y. Wang, *Nat. Catal.*, 2020, **3**, 478-487.
67. X. Ye, C. Yang, X. Pan, J. Ma, Y. Zhang, Y. Ren, X. Liu, L. Li and Y. Huang, *J. Am. Chem. Soc.*, 2020, **142**, 19001-19005.
68. C. Yang, R. Mu, G. Wang, J. Song, H. Tian, Z.-J. Zhao and J. Gong, *Chem. Sci.*, 2019, **10**, 3161-3167.
69. F. Hebrard and P. Kalck, *Chem. Rev.*, 2009, **109**, 4272-4282.
70. A. Hassan and M. A. Dar, *New J. Chem.*, 2023, **47**, 7225-7231.
71. K. Zhao, X. Nie, H. Wang, S. Chen, X. Quan, H. Yu, W. Choi, G. Zhang, B. Kim and J. G. Chen, *Nat. Commun.*, 2020, **11**, 2455.
72. G. L. Miessler, P. J. Fischer, D. A. Tarr, *Inorganic Chemistry, 5th Ed., Pearson: Boston*, 2014, 453-456.
73. F. Basolo, R. G. Pearson, *Mechanisms of Inorganic Reactions, 2nd ed., J. Wiley & Sons, New York*, 1967, 262.